Stable, Self-Adhesive, and High-Performance Graphene-Oxide-Modified Flexible Ionogel Thermoelectric Films

Shuai Sun, Xiao-Lei Shi,* Wanyu Lyu, Min Hong, Wenyi Chen, Meng Li, Tianyi Cao, Boxuan Hu, Qingfeng Liu,* and Zhi-Gang Chen*

Ionic thermoelectric materials have attracted increasing attention because of their high flexibility and high Seebeck coefficient. However, their insufficient thermoelectric performance and long-standing processing limit their practical applications. To achieve exotic ionic thermoelectric materials, here, a graphene oxide (GO) modified acrylamide ionogel is designed with high thermoelectric performance and flexibility. Detailed structural characterizations confirm that the uniform dispersion of GO particles in the ionogel structure enables a power factor of 753.0 µW m^{-1} K^{-2} and a promising *ZT* value of 0.19. Additionally, the as-prepared ionic thermoelectric thin film shows excellent flexibility, stretchability, and self-adhesiveness. An integrated device, assembled by the as-prepared ionogel films, can generate an optimal output power density of 1.32 mW cm^{-2} with a temperature difference of 20 K, indicating great potential for wearable electronics. This work provides insight for searching long-term, high-performance ionic thermoelectric materials.

S. Sun, X.-L. Shi, W. Lyu, W. Chen, M. Li, T. Cao, B. Hu, Z.-G. Chen
School of Chemistry and Physics
ARC Research Hub in Zero-emission Power Generation for Carbon Neutrality, and Centre for Materials Science
Queensland University of Technology
Brisbane, Queensland 4000, Australia
E-mail: xiaolei.shi@qut.edu.au; zhigang.chen@qut.edu.au
S. Sun, M. Hong, Z.-G. Chen
Centre for Future Materials
University of Southern Queensland
Springfield Central, Queensland 4300, Australia
W. Chen
School of Mechanical and Mining Engineering
The University of Queensland
Brisbane, Queensland 4072, Australia
Q. Liu
State Key Laboratory of Materials Oriented Chemistry Engineering
College of Chemistry Engineering
Nanjing Tech University
Nanjing 211800, China
E-mail: qfliu@njtech.edu.cn

1. Introduction

Thermoelectric materials and devices play a significant role in the development of clean energy by converting waste heat into electricity.[1–5] Generally, the performance of thermoelectric devices largely depends on the properties of the thermoelectric materials. Therefore, significant improvements in the performance of thermoelectric materials are required to enhance the output power and thermoelectric conversion efficiency of their devices.[6–8] Currently, the performance of thermoelectric materials remains a key factor limiting the practical application of thermoelectric devices, especially for flexible thermoelectric generators and coolers. The dimensionless figure-of-merit *ZT* is used to evaluate the thermoelectric performance of these materials, defined as ZT = S$^2\sigma$T/κ, where the power factor $S^2\sigma$ is composed of the Seebeck coefficient *S* and the electrical conductivity σ, *T* is the absolute temperature (K), and κ is the thermal conductivity. Currently, there are mainly three common types of thermoelectric materials: semiconductors with high *ZT* but low flexibility,[9–11] organic polymers and small molecules that exhibit high flexibility and low κ but relatively poor *S*,[12–14] and carbon-based materials with high σ and flexibility but low *S* and high κ.[15–17] Furthermore, the combination of these materials as composites is also widely studied to achieve comprehensive high performance.[18–20]

Recently, ionic thermoelectric materials have emerged as a new class of thermoelectric materials based on the Soret effect or thermochemical reactions.[21–23] The most important characteristic of ionic thermoelectric materials is their outstanding *S*, which is typically on the magnitude of millivolts per Kelvin (mV K^{-1}), ≈10–100 times higher than that of traditional thermoelectric materials.[24–26] Additionally, ionic thermoelectric materials possess excellent flexibility and stretchability, making them considered as thermoelectric materials with practical application potential.[27,28] Ionic thermoelectric materials can be utilized in flexible thermoelectric devices to harness power from irregular heat sources. In most cases, ionic thermoelectric materials are composed of various functional components. Among them, the ionic donor is the most important, providing ion carriers such as ionic liquids, polyelectrolytes, and so on.[29,30]

ADVANCED
SCIENCE NEWS

www.advancedsciencenews.com

ADVANCED
FUNCTIONAL
MATERIALS

www.afm-journal.de

Meanwhile, the framework matrix is typically an organic polymer, such as bacterial cellulose, and gelatin.[31–33] Additionally, organic solvents and water are used to facilitate ion migration and gel swelling.[34,35] However, a major drawback arising from this is instability, specifically the non-uniformity of solvents over an extended period. For instance, in unsealed ion gel/water gel-based ionic thermoelectric materials, both flexibility and thermoelectric performance (particularly σ) may experience degradation within several hours.[23,36–38] Moreover, the larger volume and higher transfer entropy of ion carriers can also lead to a decrease in σ.[26] With some recent advancements in ionic thermoelectric research, several preliminary strategies have been developed to overcome this challenge. For example, a ternary hybrid of poly(2-acrylamido-2-methyl-1-propanesulfonic acid) (PAAMPSA)/phytic acid (PA)/polyaniline (PANI) exhibited excellent σ of 256.0 mS cm^{-1} at 90% relative humidity (RH).[27] By combining the ion conductivity of PAAMPSA/PA with the electronic conductivity of PANI, σ was improved by 33% compared to the original PAAMPSA/PA. However, most strategies aimed at promoting ion concentration/mobility remain highly sensitive to humidity or solvent composition. The acid gradient of PA is also limited in the fabrication of electronic skin devices.

Carbon-based materials exhibit significant potential in the field of flexible thermoelectrics.[39] Carbon-based materials possess high intrinsic σ, which theoretically can compensate for the lower σ of ionic thermoelectric materials.[40,41] However, achieving uniform dispersion of inorganic carbon-based particles within organic-based ionic thermoelectric materials is still challenging.[42–44] Therefore, one of the aims is to achieve a continuous carbon phase to improve the overall σ, which is difficult to accomplish with particle-level dispersion.[45,46] However, because water may be an essential component of the ionic thermoelectric system, we have noticed that graphene oxide (GO) exhibits high water solubility.[47,48] Although the intrinsic σ of GO (>10 mS cm^{-1}) is not as high as graphene and carbon nanotubes, it still falls within the same magnitude as that of ionic thermoelectric materials.[49,50] This provides a new approach for designing ionic thermoelectric materials with high stability and high thermoelectric performance.

In this study, we developed a GO-blended polyacrylamide (PAM) ionic thermoelectric thin film that simultaneously exhibited high stability, competitive thermoelectric performance, and excellent flexibility. **Figure 1a** illustrates the fabrication process of the film, from which the raw materials include acrylamide (AM), 1-butyl-3-methylimidazolium chloride (BMIM:Cl), initiator ammonium persulfate (APS), and crosslinker N,N'-methylenebisacrylamide (MBA) in a mixed solution. The initiator is crucial for the dispersion of GO while the crosslinker is essential for the mechanical properties of the prepared film. Our optimized film (PAM$_{0.3}$-BMIM:Cl$_{0.6}$-GO$_1$) achieved an outstanding S value of -76.7 mV K^{-1} and a promising ZT of 0.19 at 0% humidity and 383 K, surpassing most reported ionic thermoelectric materials, as indicated by Figure 1b,c.[21,29,51–57] Additionally, the as-prepared film exhibited exceptional stability even after 7 days of exposure in the air. Furthermore, the tensile strength, elongation at break, Young's modulus, toughness, and flexibility of the as-prepared film reached 219.7 kPa, 389%, 84.1 kPa, 0.4 MJ m^{-3}, and 180° bending, respectively, ranking among the top in existing ionic thermoelectric materials.[51,58,59] Based on

its high thermoelectric and mechanical properties, we manufactured a 25×25 mm^2 flexible device with 9 legs through an integration strategy. It can generate an optimal output power density ω_{max} of 1.32 mW cm^{-2} with a temperature difference ΔT of 20 K. This design is crucial for advancing the research on ionic flexible thermoelectric materials and devices.

2. Results and Discussion

In the typical fabrication, GO solution was added to the pre-prepared solution and then subjected to ultrasonic dispersion in an ice-water bath. The ice-water bath was critical for the good dispersion of GO. After the synthesis of the ion gel by free-radical polymerization at 333 K, the film material was annealed for 5 h at 383 K, which was vital for the stability of the prepared film. After achieving the films, we first analyzed the thermoelectric performance and stability of PAM$_{0.3}$-BMIM:Cl$_{0.6}$-GO$_x$ (subscripts represent the mass ratio of PAM, BMIM:Cl, and the 2 mg mL^{-1} GO solution, Table S1, Supporting Information) to find the optimal composition (x value). The σ and S measurements were conducted using the direct-current (DC) four-probe method and the short-time voltage capture method, respectively (instruments can be referenced from Figure S1, Supporting Information). This choice is informed by our observation of continuous power supply over 120 min, as depicted in Figure S2 (Supporting Information). Consequently, we deem the as-prepared PAM$_{0.3}$-BMIM:Cl$_{0.6}$-GO$_x$ more suitable for serving as a DC-mode power generator.

After detailed characterizations, the optimal composition of PAM$_{0.3}$-BMIM:Cl$_{0.6}$ can be fixed with a ratio of 1:2 (0.3:0.6) as it exhibits the best thermoelectric performance (Table S2, Supporting Information). Theoretically, the higher the proportion of the BMIM:Cl ionic liquid, the better the thermoelectric performance. However, the ratio of 1:2 (PAM$_{0.3}$-BMIM:Cl$_{0.6}$) represents an upper limit, as exceeding this ratio would make it difficult to stably incorporate a larger amount of BMIM:Cl within the film, as shown in the photos in Table S2 (Supporting Information). **Figure 2a** compares room-temperature σ and S. With increasing the x value, the σ was increased from 2.2 to 5.9 mS cm^{-1}, and the S was decreased from -33.8 to -30.1 mV K^{-1}. It has been reported that pure GO has a typical σ value of >10 mS cm^{-1}.[49,50,61] Herein, we initially measured the intrinsic σ of the commercial GO (by drop-casting a thin film) to be 24.3 mS cm^{-1} (Figure S3, Supporting Information). Therefore, after mixing with GO, both ions and electronic charge carriers contribute to optimized σ. Moreover, it is known that the σ of ionic thermoelectric materials is highly sensitive to humidity, and high humidity is necessary for high σ performance.[26,62] In this work, the σ testing was conducted under a high-vacuum environment, which can be considered as 0% humidity. Therefore, achieving a σ as high as 5.9 mS cm^{-1} under such conditions is highly promising. Furthermore, increasing the GO content results in a slight decrease in S. On one hand, well-dispersed GO can slightly impede the transport of ion charge carriers; on the other hand, the interaction between GO and EMIM$^+$ plays an important role in improving the balanced EMIM$^+$/Cl$^-$ concentration gradients, enhancing the S.[63] The slight decrease in S is likely a result of the combined effects of these two factors. Additionally, it should be noted that PAM$_{0.3}$-BMIM:Cl$_{0.6}$-GO$_x$ is an n-type ionic
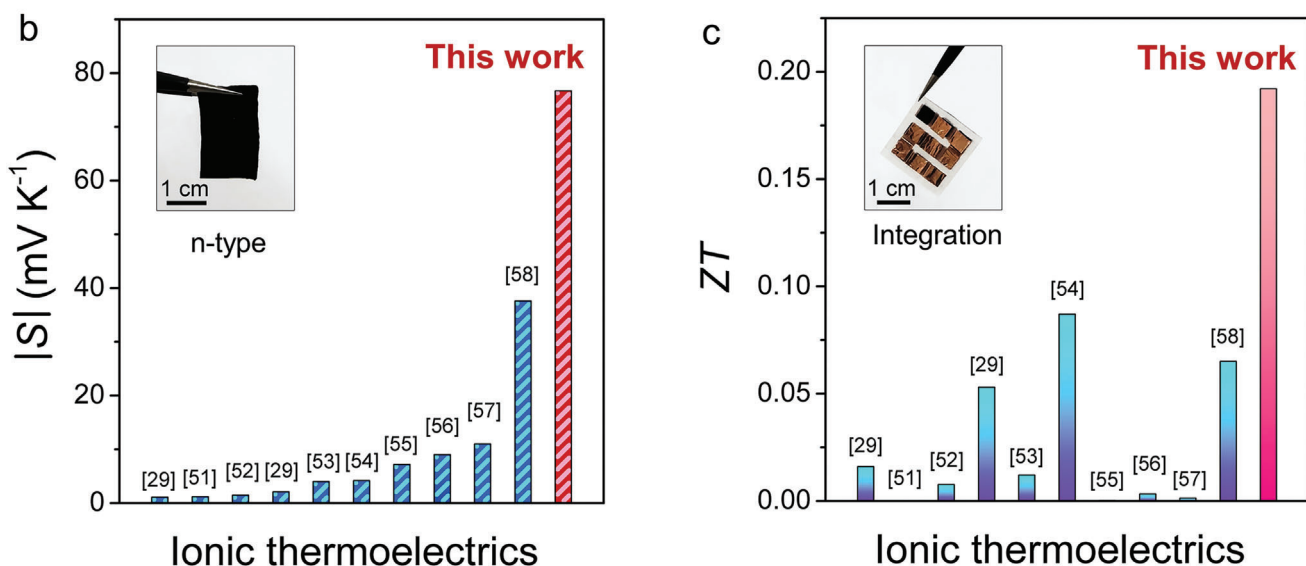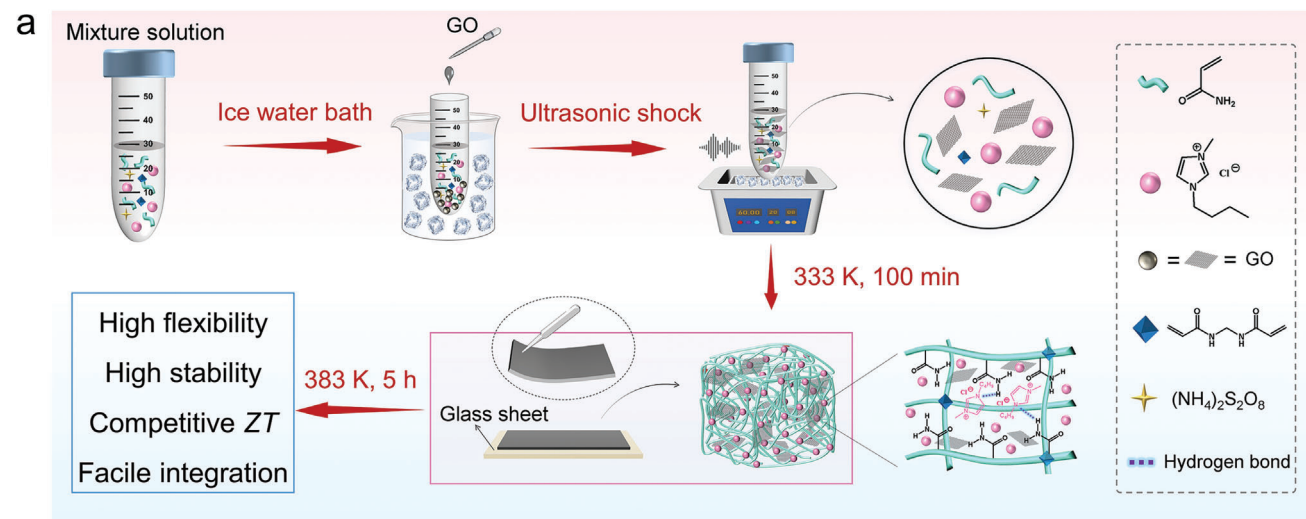
**ADVANCED
SCIENCE NEWS**

www.advancedsciencenews.com

**ADVANCED
FUNCTIONAL
MATERIALS**

www.afm-journal.de

Figure 1. Illustration of the fabrication process of $PAM_{0.3}$-BMIM:$Cl_{0.6}$-GO_x ionic thermoelectric films and their competitive thermoelectric performance. a) Schematic diagram illustrating the raw materials, fabrication process, and components of the $PAM_{0.3}$-BMIM:$Cl_{0.6}$-GO_x ionic thermoelectric film. Here PAM is abbreviated from polyacrylamide, BMIM:Cl is abbreviated from 1-butyl-3-methylimidazolium chloride, and GO is abbreviated from graphene oxide. Comparison of the optimized b) Seebeck coefficient S and c) dimensionless figure-of-merit ZT values between $PAM_{0.3}$-BMIM:$Cl_{0.6}$-GO_1 developed in this work and previously reported flexible ionic thermoelectric materials.[29,51–57,60] Inserted: photos of as-prepared b) $PAM_{0.3}$-BMIM:$Cl_{0.6}$-GO_1 film and c) thermoelectric device, respectively.

thermoelectric material, which is defined by the negative sign of S. In most cases, if anion carriers migrate dominantly to the cold end, negative S will be achieved.[26,64] Figure 2b plots the $S^2\sigma$ of $PAM_{0.3}$-BMIM:$Cl_{0.6}$-GO_x ($x = 0$, 0.2, 0.4, 0.6, 0.8, and 1). With increasing the GO content, the $S^2\sigma$ was increased. The optimal $S^2\sigma$ value was achieved with $PAM_{0.3}$-BMIM:$Cl_{0.6}$-GO_1, corresponding to 534.5 μW m^{-1} K^{-2}.

In the preparation process of $PAM_{0.3}$-BMIM:$Cl_{0.6}$-GO_x, we employed an annealing process to remove uneven H_2O components and validate their stability. To assess the efficiency, we compared the σ, S, and $S^2\sigma$ of the non-annealed film, the annealed film (final product of this work), the self-adhesive film (defined as cutting the annealed $PAM_{0.3}$-BMIM:$Cl_{0.6}$-GO_1 film into two pieces

and separating from each other, and reattaching the two pieces again by the self-adhesivity at room temperature), and the annealed film left in the air for 7 days, as shown in Figure 2c,d. The cutting process can be referred to Movie S1 (Supporting Information). It can be observed that the annealing process resulted in a slight increase in σ, an obvious improvement in S, and in turn an enhancement in $S^2\sigma$ for the as-prepared $PAM_{0.3}$-BMIM:$Cl_{0.6}$-GO_1. However, the high σ of non-annealed $PAM_{0.3}$-BMIM:$Cl_{0.6}$-GO_1 mostly originated from the BMIM:Cl dissolved in H_2O, whereas σ of annealed $PAM_{0.3}$-BMIM:$Cl_{0.6}$-GO_1 originated from the GO. Additionally, the thermoelectric performance of the as-prepared $PAM_{0.3}$-BMIM:$Cl_{0.6}$-GO_1 was highly stable. Long-term stability remains one of the key challenges for quasi-solid-state

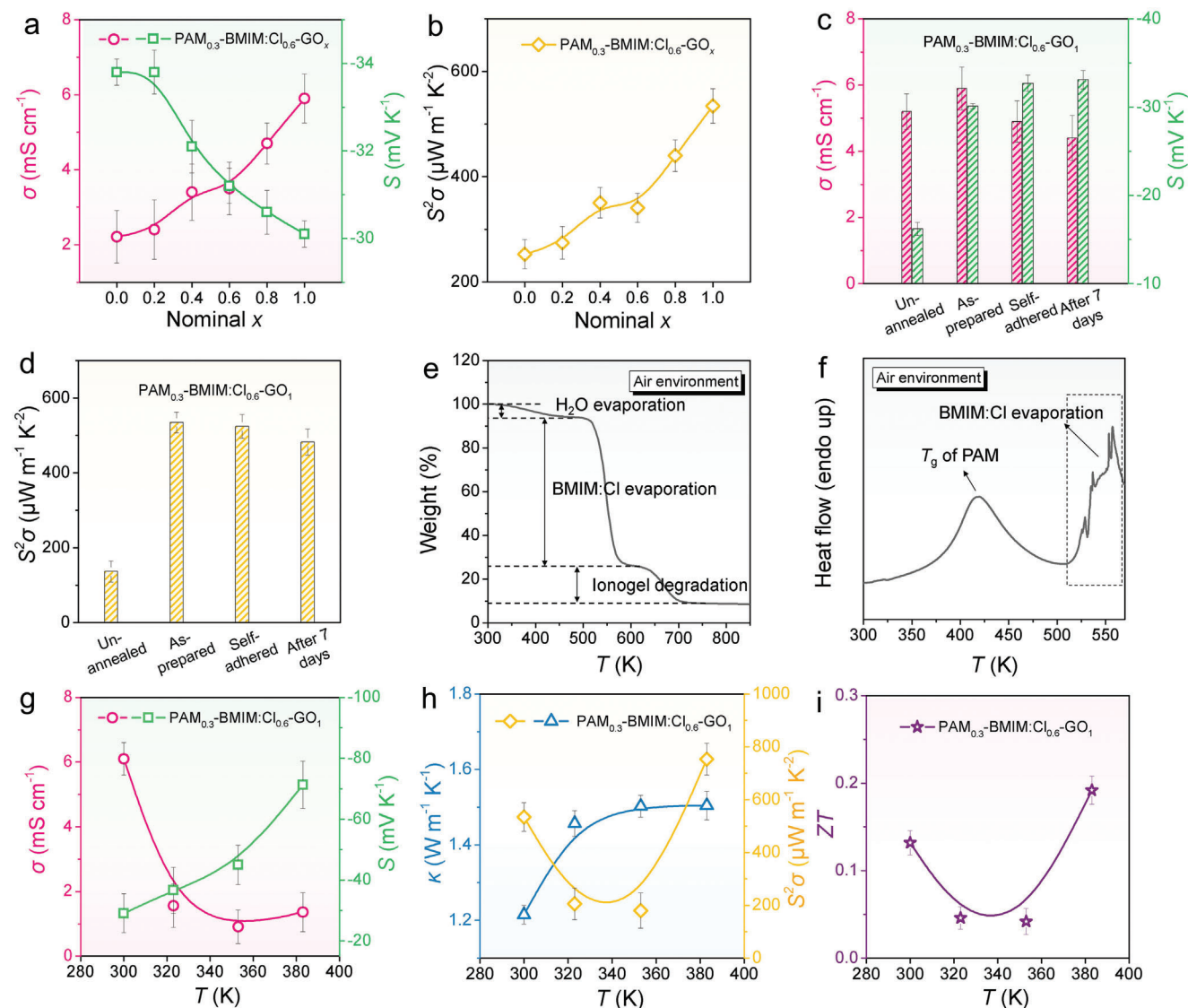**Figure 2.** Thermoelectric performance and stability of $PAM_{0.3}$-BMIM:$Cl_{0.6}$-GO_x films with different x values and working temperatures. Room-temperature a) electrical conductivity σ and S, and b) power factor $S^2\sigma$ of $PAM_{0.3}$-BMIM:$Cl_{0.6}$-GO_x (x = 0, 0.2, 0.4, 0.6, 0.8, and 1). Room-temperature c) σ and S, and d) $S^2\sigma$ of $PAM_{0.3}$-BMIM:$Cl_{0.6}$-GO_1 films for unannealed, as-prepared, self-adhered, and 7-days exposed in the air. e) Thermogravimetric analysis (TGA) and f) differential scanning calorimetry (DSC) curves of $PAM_{0.3}$-BMIM:$Cl_{0.6}$-GO_1 film in the air environment. Temperature-dependent (298–383 K) g) σ and S, h) $S^2\sigma$ and thermal conductivity κ, and i) ZT of $PAM_{0.3}$-BMIM:$Cl_{0.6}$-GO_1.

(hydrogel and ionogel) thermoelectric materials.[65,66] After self-adhesion, the $S^2\sigma$ was changed from 534.5 to 524.0 µW m^{-1} K^{-2}, and after being placed in the air for 7 days, the $S^2\sigma$ remained at 482.1 µW m^{-1} K^{-2}. Such performance was well-maintained, which holds significant importance for the practical application of ionic thermoelectric materials and devices.

To validate the thermal stability of the as-prepared $PAM_{0.3}$-BMIM:$Cl_{0.6}$-GO_1, we performed thermogravimetric analysis (TGA) and differential scanning calorimetry (DSC) tests, and the results are shown in Figure 2e,f. Figure 2e reveals three stages of mass loss: first, water (H_2O) evaporated in the temperature range of 300–446 K; second, BMIM:Cl evaporated in the range of 515–580 K; and finally, the degradation of $PAM_{0.3}$-BMIM:$Cl_{0.6}$-GO_1 ionogel started at ≈640–700 K. Since the sample was annealed

at 383 K for 5 h, the H_2O component should be saturated absorption from the air, accounting for 6 wt%. For comparison, the TGA curve of non-annealed $PAM_{0.3}$-BMIM:$Cl_{0.6}$-GO_1 is shown in Figure S4 (Supporting Information), where the H_2O proportion was increased to 48 wt%. However, the absorption of H_2O in the air is inevitable for the hydrophilic PAM component, and theoretically, it would not affect the high-vacuum thermoelectric performance discussed in this work. In Figure 2f, the DSC curve of $PAM_{0.3}$-BMIM:$Cl_{0.6}$-GO_1 displays the glass transition temperature T_g of the PAM component to be ≈418 K. Furthermore, the irregular exothermic peak after 515 K is attributed to the evaporation of BMIM:Cl, consistent with the second mass loss observed in Figure 2e. Figure S5 (Supporting Information) demonstrates the temperature-dependent (300–500 K) complex viscosity,

**ADVANCED
SCIENCE NEWS**

www.advancedsciencenews.com

**ADVANCED
FUNCTIONAL
MATERIALS**

www.afm-journal.de

storage modulus, and loss modulus of $PAM_{0.3}$-$BMIM:Cl_{0.6}$-GO_1 film, where a coincided phase transition point (T_g) is observed at 385 K.

Considering the study of the temperature resistance of the ionic thermoelectric thin film and its potential application in high-temperature scenarios, we investigated the thermoelectric performance of the as-prepared $PAM_{0.3}$-$BMIM:Cl_{0.6}$-GO_1 in the temperature range of 298–383 K, as shown in Figures 2g–i and Figure S6 (Supporting Information). Before 353 K, with increasing the temperature, the σ was decreased while the S was increased, as depicted in Figure 2g. However, when the temperature reached 383 K, the σ was slightly increased and the S was dramatically increased. This is attributed to the enhanced charge carrier mobility, which can be conferred by the PAM molecular segments thawing from freezing (approaching the T_g point). Around this phase transition point of the abundant component PAM, ion carrier migration increase will be dramatic enough to facilitate S.[67,68] Similar carrier mobility and ionic S improvements with improved temperature have been reported in the literature.[68–72] Additionally, polymer-based ionogel materials typically exhibit low κ.[26] Moreover, the annealing process reduces the liquid content of the as-prepared $PAM_{0.3}$-$BMIM:Cl_{0.6}$-GO_1, limiting convective heat transfer. As a result, the κ value ranges from 1.22 to 1.50 W m^{-1} K^{-1} in the temperature range of 298–383 K. Consequently, the $S^2\sigma$ of the prepared $PAM_{0.3}$-$BMIM:Cl_{0.6}$-GO_1 reaches 753.0 μW m^{-1} K^{-2} at 383 K with a ZT of 0.19. Such temperatures can be widely obtained from industrial circulating cooling water in practical applications. Although the ZT values are not widely applied for ionic thermoelectric materials, they still provide valuable references.

Since $PAM_{0.3}$-$BMIM:Cl_{0.6}$-GO_x is a ternary hybrid material, we utilized Fourier-transform infrared reflectance (FT-IR), X-ray diffraction (XRD), Raman spectroscopy, and X-ray photoelectron spectroscopy (XPS) to study the different components within the film and their interactions. During the preparation process, PAM was synthesized via free-radical polymerization at 333 K (Figure 1a). To validate the polymerization efficiency, the FT-IR results of the original GO, $PAM_{0.3}$-$BMIM:Cl_{0.6}$ film, annealed $PAM_{0.3}$-$BMIM:Cl_{0.6}$-$GO_{0.4}$ film, annealed $PAM_{0.3}$-$BMIM:Cl_{0.6}$-GO_1 film (final product in this work), and non-annealed $PAM_{0.3}$-$BMIM:Cl_{0.6}$-GO_1 film are shown in **Figure 3a**. From the spectra, the four film samples exhibit similar peak characteristics, consistent with typical PAM spectra. The single peaks observed ≈3360 and 1660 cm^{-1} can be attributed to the stretching vibrations of N—H and C=O in PAM.[73] Besides, peaks at 1570 and 1455 cm^{-1} are attributed to the stretching vibrations of C=N and bending vibration of C=H from BMIM:Cl components.[74] Therefore, the introduction of BMIM:Cl and GO did not disrupt the synthesis of PAM. Additionally, the structure of BMIM:Cl in the ternary hybrid $PAM_{0.3}$-$BMIM:Cl_{0.6}$-GO_x remained intact. Here, with the addition of GO, a new peak appeared at 2140 cm^{-1}. This is likely attributed to the conjugation effect between the imidazole ring and GO.[75,76]

Due to the extremely low content of pure GO (e.g., ≈0.22 wt% relative to the total mass of annealed $PAM_{0.3}$-$BMIM:Cl_{0.6}$-GO_1, as shown in Table S1, Supporting Information), we employed XRD to characterize the state of GO. As shown in Figure 3b, the original GO, annealed $PAM_{0.3}$-$BMIM:Cl_{0.6}$-$GO_{0.4}$, and annealed $PAM_{0.3}$-$BMIM:Cl_{0.6}$-GO_1 exhibit broad peaks at ≈16.8°,

while the original $PAM_{0.3}$-$BMIM:Cl_{0.6}$ as an amorphous polymer material does not show any distinct crystalline peaks.[77] The consistent peak positions of the original GO, annealed $PAM_{0.3}$-$BMIM:Cl_{0.6}$-$GO_{0.4}$, and annealed $PAM_{0.3}$-$BMIM:Cl_{0.6}$-GO_1 indicate good preservation of the hybridized crystalline phase and interlayer spacing. Interestingly, the characteristic peaks related to GO diffraction disappear in the non-annealed $PAM_{0.3}$-$BMIM:Cl_{0.6}$-GO_1, suggesting that the presence of H_2O impedes the crystallinity of GO. This is further supported by the Raman spectra shown in Figure 3c, where the appearance of the characteristic G and D bands with increasing GO content indicates a physical blending.[78,79] However, Raman absorption is blocked by highly flowable H_2O regarding unannealed $PAM_{0.3}$-$BMIM:Cl_{0.6}$-GO_1.

To investigate the elemental composition and valency states, the XPS spectra are shown in Figure 3d,e and Figure S7 (Supporting Information). According to the peaks of Cl2s (194.0 eV) and Cl2p (264.9 eV) (Figure S7 and Table S3, Supporting Information),[80,81] the BMIM:Cl components are successfully introduced into the as-prepared $PAM_{0.3}$-$BMIM:Cl_{0.6}$-GO_x. However, even though the binding energy of Cl2p remains constant for $PAM_{0.3}$-$BMIM:Cl_{0.6}$ and as-prepared $PAM_{0.3}$-$BMIM:Cl_{0.6}$-GO_1 (Figure 3d), a blue shift phenomenon can be observed for the N1s peak of $PAM_{0.3}$-$BMIM:Cl_{0.6}$-GO_1 compared with $PAM_{0.3}$-$BMIM:Cl_{0.6}$ (Figure 3e).[82] Considering that the Cl element is only presented in the BMIM:Cl component and the N element is presented in both the PAM and BMIM:Cl components, it can be confirmed that there is a binding interaction between GO and both BMIM$^+$ and PAM amino groups. Additionally, the presence of N in the original GO film is attributed to the oxygen functional groups. As a result, Figure 3f describes the schematic diagram of the interaction between GO and BMIM$^+$. As widely reported, the generation of the ionic thermoelectric effect relies on differences in ion concentration and diffusion rates between cations and anions.[26] Specifically, both BMIM$^+$ and Cl$^-$ particles are prone to migrate from the hot side to the cold side under a ΔT, followed by accumulating at the cold electrode surface. The original S can be attributed to the migration efficiency difference between small-sized Cl$^-$ and large-sized BMIM$^+$. After the hybridization with GO, BMIM$^+$ can be dragged by the GO component in the film bulk.[63,83] As a result, a better decoupling effect and a higher migration rate difference between Cl$^-$ and EMIM$^+$ can be achieved. After reaching diffusion equilibrium, a superior carrier concentration difference between Cl$^-$ and EMIM$^+$ appears on the cold side, resulting in improved S.

To assess the dispersion of GO, we conducted scanning electron microscopy (SEM) and energy-dispersive X-ray spectroscopy (EDS) analysis, and the results are presented in **Figure 4**. Due to the annealing process, the surface of the $PAM_{0.3}$-$BMIM:Cl_{0.6}$-GO_1 film exhibits uniform micro-wrinkles (Figure 4a). However, the width of the wrinkles is ≈1 μm (Figure 4b), which is sufficiently narrow and does not affect the overall morphology of the film. Furthermore, the backscattered electron (BSE) imaging mode shown in Figure 4c confirms the uniform dispersion of the PAM, BMIM:Cl, and GO components.[84,85] The EDS results in Figure 4d,e demonstrate the uniform distribution of C, N, O, and Cl elements. The elemental spectrum in f provides the specific ratios of N, O, and Cl (Pt is the coating material used for SEM sample preparation). For comparison, the corresponding
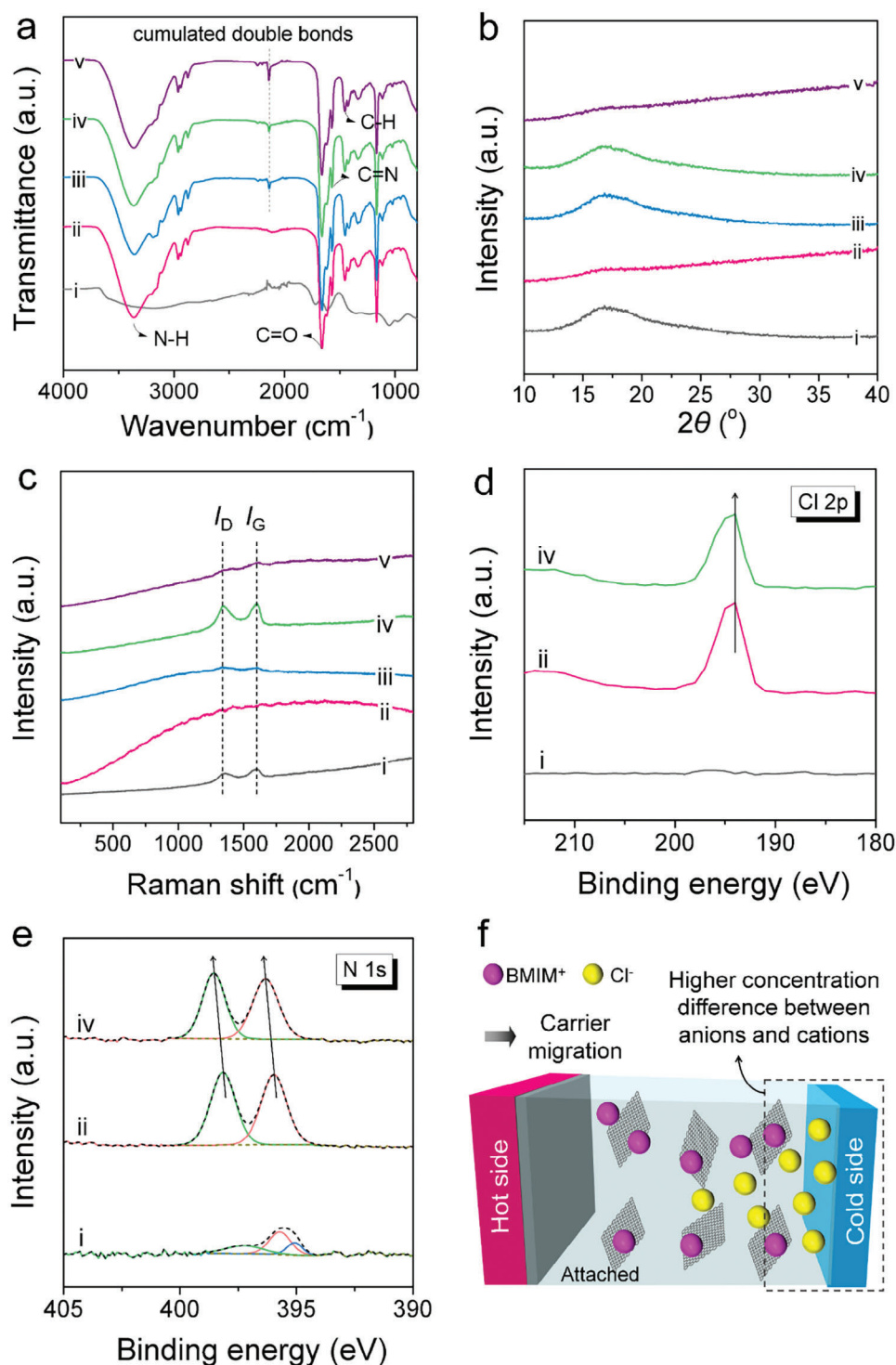
Figure 3. Characterizations of structure, atom binding information of i) pristine GO, ii) $PAM_{0.3}$-$BMIM$:$Cl_{0.6}$, iii) annealed $PAM_{0.3}$-$BMIM$:$Cl_{0.6}$-$GO_{0.4}$, iv) annealed $PAM_{0.3}$-$BMIM$:$Cl_{0.6}$-GO_1 (final product in this work), and v) unannealed $PAM_{0.3}$-$BMIM$:$Cl_{0.6}$-GO_1, and schematic diagram of carrier transfer of the hybrid films. a) Attenuated total reflectance Fourier transform infrared reflection (ATR-FTIR) spectra. b) X-ray diffraction (XRD) pattern. c) Raman pattern. d) X-ray photoelectron spectroscopy (XPS) patterns with corresponding magnified Cl2p patterns and e) magnified N1s patterns. f) Schematic diagram showing the interaction between GO and $BMIM^+$, and the resulted higher difference in carrier concentration after GO hybridization.
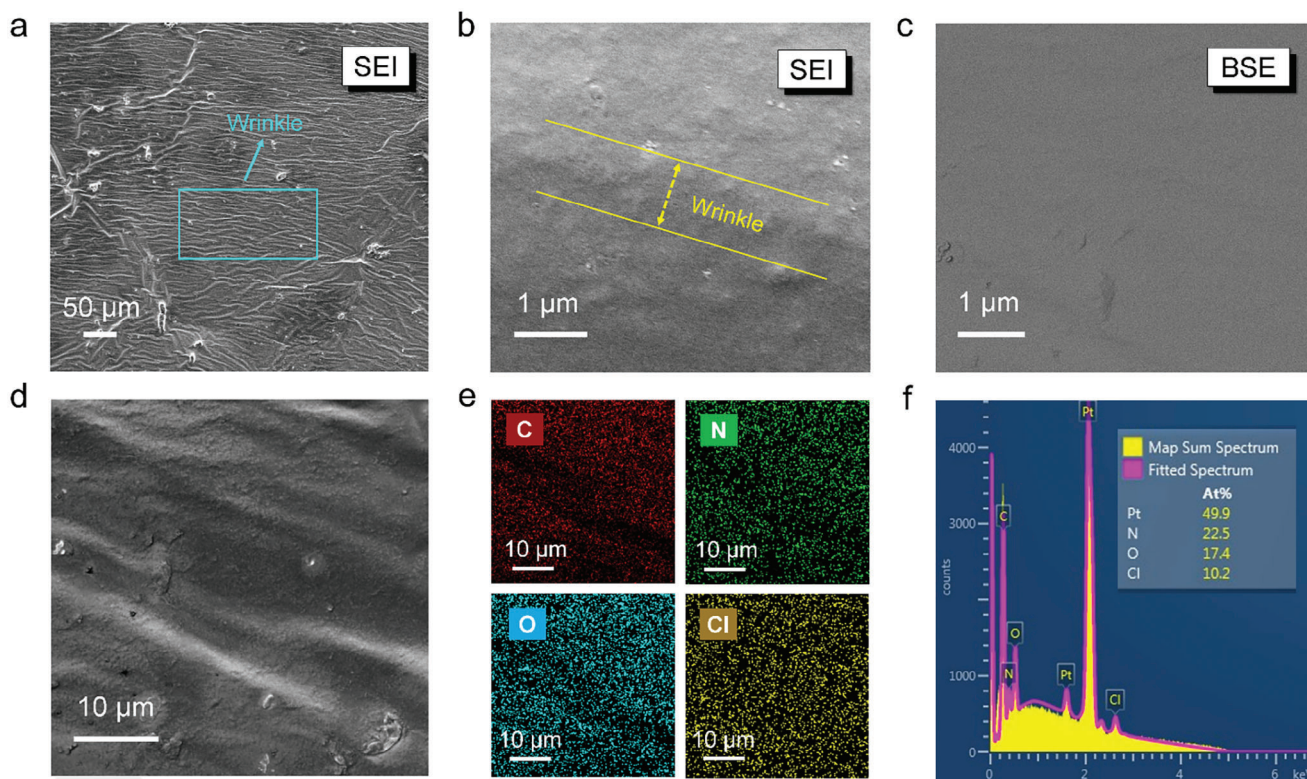
ADVANCED
SCIENCE NEWS

www.advancedsciencenews.com

ADVANCED
FUNCTIONAL
MATERIALS

www.afm-journal.de

Figure 4. Characterizations of surface morphology and element distributions of as-prepared $PAM_{0.3}$-$BMIM{:}Cl_{0.6}$-GO_1 film. Scanning electron microscopy (SEM) images of $PAM_{0.3}$-$BMIM{:}Cl_{0.6}$-GO_1 with a) low- and b) high-magnification secondary electron imaging (SEI) modes, c) high-magnification backscattered electron imaging (BSE) mode. d) SEM image, e) corresponding X-ray spectroscopy (EDS) mapping images for C, N, O, and Cl elements, and f) corresponding EDS element spectra of a random area of $PAM_{0.3}$-$BMIM{:}Cl_{0.6}$-GO_1.

elemental mapping and ratio information of the film after 7 days are shown in Figure S8 (Supporting Information). The uniform elemental distribution and unchanged elemental ratios confirm the exceptional stability of the prepared $PAM_{0.3}$-$BMIM{:}Cl_{0.6}$-GO_1 film.

The mechanical properties, especially flexibility, are crucial for the practical applications of thermoelectric films. To study the mechanical performance at a constant room RH of 50%, the tensile curves of the $PAM_{0.3}$-$BMIM{:}Cl_{0.6}$-GO_1 film before and after annealing are shown in **Figure** 5a. Compared to the non-annealed film, the annealed film as the final product exhibits a 103% increase in tensile strength, while the fracture elongation remains nearly unchanged. The inset demonstrates that a lemon weighing 1.2 N can be supported by the film with a dimension of $20 \times 5 \times 1$ mm³. Furthermore, we conducted repeated tensile tests for 5 cycles using recovered fractured film segments (randomly selected from fractured samples). As shown in Figure 5b, with increasing test cycles, although the tensile performance was decreased, the prepared film still demonstrates potential for repeated use. To measure the long-term application potentials, Figure S9 (Supporting Information) shows the tensile curves of repeating 100% stretching for 1, 20, and 52 cycles. The tensile strength of the $PAM_{0.3}$-$BMIM{:}Cl_{0.6}$-GO_1 film was well-maintained after 52 cycles. Although the strip-like sample broke after 52 cycles, this stretching behavior is still considerable for practical applications. Overall, the mechanical properties of the film, including 219.7 kPa tensile strength, 389% fracture elongation, 84.1 kPa Young's modulus, 0.4 MJ m⁻³ toughness, and 180° bending angle, are all highly competitive among reported ionic thermoelectric films (Figure 5c; Table S4, Supporting Information).[51,58,59] The photographs of the original, curled, and stretched $PAM_{0.3}$-$BMIM{:}Cl_{0.6}$-GO_1 film in the air (Figure 5d) and on the ice (Figure 5e) provide visual evidence of the high flexibility. Additionally, our film exhibits suitable self-adhesiveness, where the tested experimental RH was 50%. After bonding, plastics, metals, and wood can be suspended using a film measuring $20 \times 5 \times 1$ mm³ under a load of 500 N (Figure 5f). The self-adhesive property is highly advantageous for device fabrication as electrode materials can be directly adhered to the film.

Based on the high thermoelectric performance, flexibility, stability, and self-adhesive features of the as-prepared $PAM_{0.3}$-$BMIM{:}Cl_{0.6}$-GO_1 film, we devised a method for integrating small-sized flexible thermoelectric devices. We first tested a single-leg film as indicated by the demonstration video (Movie S2, Supporting Information), showing the output performance. Moreover, it should be noted that the single-leg $PAM_{0.3}$-$BMIM{:}Cl_{0.6}$-GO_1 film successfully achieves 120 min of long-term steady power generation (Figure S2, Supporting Information). This characteristic ensures the potential operational mode of a thermoelectric generator for $PAM_{0.3}$-$BMIM{:}Cl_{0.6}$-GO_1. Based on this, as shown in **Figure** 6a, a liquid mixed solution containing AM, BMIM:Cl, GO, initiator, and cross-linker was dispensed onto a 1 mm-thick
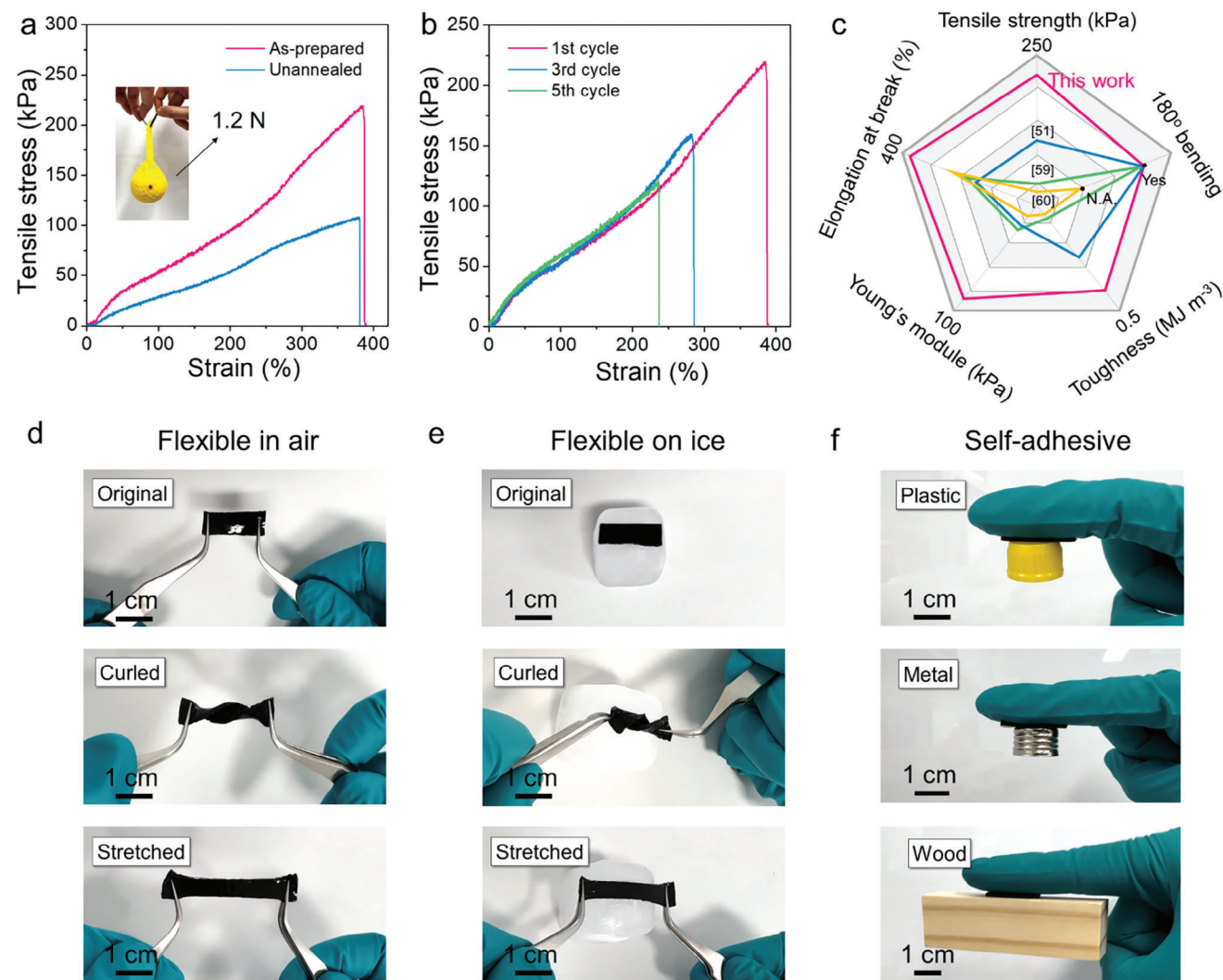
Figure 5. Characterizations of mechanical properties and flexibilities of $PAM_{0.3}$-$BMIM{:}Cl_{0.6}$-GO_1 films. Tensile curves (at a constant relative humidity, RH, of 50%) of a) as-prepared and unannealed $PAM_{0.3}$-$BMIM{:}Cl_{0.6}$-GO_1 films, the inserted image shows a $20 \times 5 \times 1$ mm^3 film (as-prepared $PAM_{0.3}$-$BMIM{:}Cl_{0.6}$-GO_1) lifting a 1.2 N weighted lemon, b) as-prepared $PAM_{0.3}$-$BMIM{:}Cl_{0.6}$-GO_1 films at the 1st, 3rd, and 5th testing cycle, respectively. c) Comparison of the tensile strength, elongation at break, Young's module, toughness, and 180° bending angle between as-prepared $PAM_{0.3}$-$BMIM{:}Cl_{0.6}$-GO_1 film and reported ionic thermoelectric films reported in literature.[51,58,59] Images showing the original, curled, and stretched state of as-prepared $PAM_{0.3}$-$BMIM{:}Cl_{0.6}$-GO_1 film d) in the air and e) on the ice. f) Images showing the self-adhesivity of $PAM_{0.3}$-$BMIM{:}Cl_{0.6}$-GO_1 film at an RH of 50%, which slings plastic, metal, and wood under 500 N.

custom-made organosilicon film. After curing and annealing processes, a 9-leg device was integrated. Subsequently, copper foil electrodes were directly adhered to the surface of $PAM_{0.3}$-$BMIM{:}Cl_{0.6}$-GO_1 through end-to-end connections. Finally, two pieces of polyimide tape were used as encapsulation layers, resulting in a π-shaped flexible thermoelectric device.[86] The fabricated flexible device is shown in Figure 6b and Figure S10 (Supporting Information), and the overall device size (25×25 mm) has been miniaturized to approach the size of a coin (Figure 6c). The output performances of the 9-leg device are shown in Figure 6d–f and Figure S11 (Supporting Information). During the waved temperature loadings, our device exhibits good cyclic performance as the temperature difference (ΔT) transforms (Figure S11, Supporting Information). The output voltage

(V) (Figure S11b, Supporting Information) curve matches the ΔT curve (Figure S11a, Supporting Information) without obvious postponing. Figure 6d displays the V of $PAM_{0.3}$-$BMIM{:}Cl_{0.6}$-GO_1 and $PAM_{0.3}$-$BMIM{:}Cl_{0.6}$ based thermoelectric devices, respectively, as a function of the loading current I_{load} at different ΔTs ($\Delta T = 10$ and 20 K). Linearly matched V-I_{load} plots are obtained for the $PAM_{0.3}$-$BMIM{:}Cl_{0.6}$-GO_1 and $PAM_{0.3}$-$BMIM{:}Cl_{0.6}$ based devices, showing their stable resistances. The corresponding output power P ($P = V \times I_{load}$) was calculated and shown in Figure 6e. With the same ΔT, the $PAM_{0.3}$-$BMIM{:}Cl_{0.6}$-GO_1 based device exhibits much higher P values than that of the $PAM_{0.3}$-$BMIM{:}Cl_{0.6}$-based device, verifying the GO addition effectively improves the device power generation. Figure 6f shows the corresponding maximum output power density ω_{max} with ΔTs of 10

**ADVANCED
SCIENCE NEWS**

www.advancedsciencenews.com

**ADVANCED
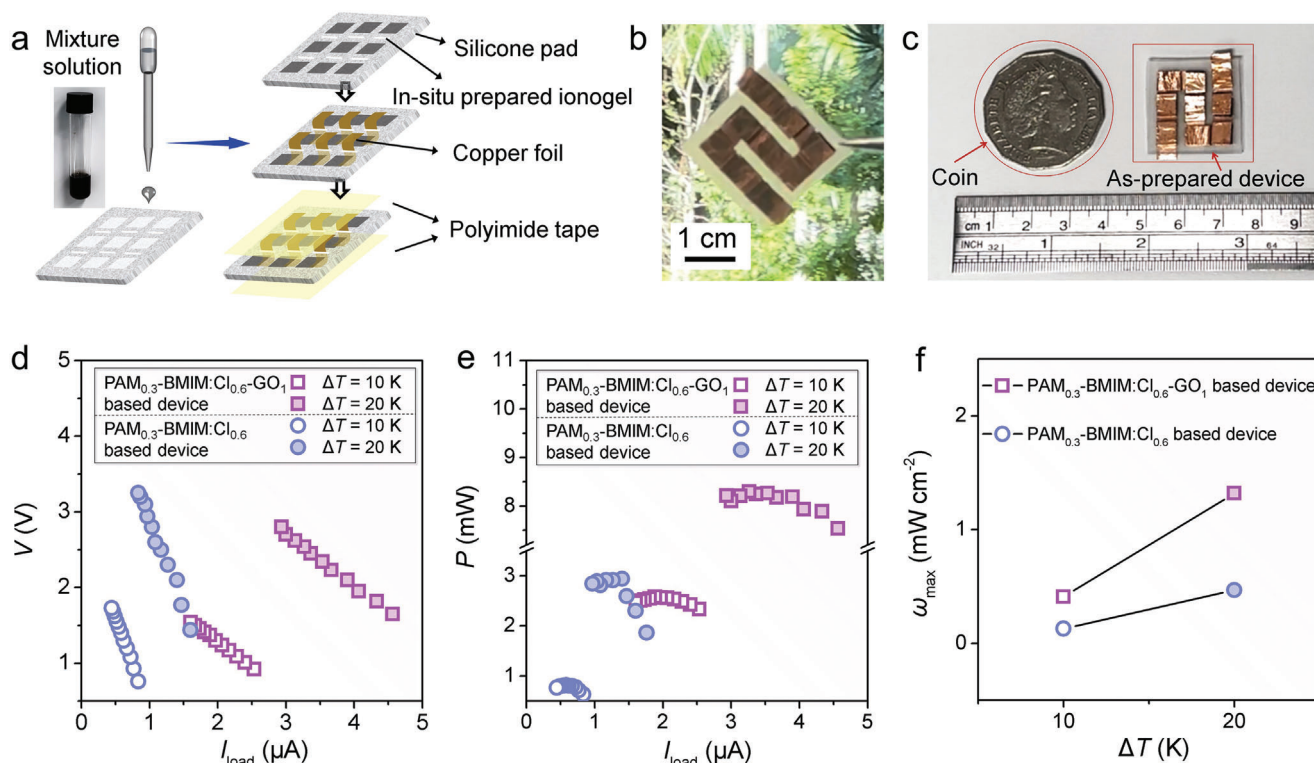FUNCTIONAL
MATERIALS**

www.afm-journal.de

Figure 6. Preparation and the output performance comparisons of PAM$_{0.3}$-BMIM:Cl$_{0.6}$-GO$_1$ based thermoelectric device. a) Schematic diagram of the integration, physical connection, and structure of the device. b) Photo of the connected 9-leg 25 × 25 mm^2 flexible device. c) Photo compared the miniaturized size of the prepared device and a coin. d) Output voltage V and e) calculated output power P of PAM$_{0.3}$-BMIM:Cl$_{0.6}$-GO$_1$ and PAM$_{0.3}$-BMIM:Cl$_{0.6}$ based thermoelectric devices as a function of the loading current I_{load} (at temperature difference ΔT of 10 and 20 K respectively). Here two heating stages act as thermal sources, and the data were acquired by keeping the cold-side temperature T_c at 300 K. f) Calculated maximum output power density ω_{max} as a function of ΔT for PAM$_{0.3}$-BMIM:Cl$_{0.6}$-GO$_1$ and PAM$_{0.3}$-BMIM:Cl$_{0.6}$ based thermoelectric devices. Note: the connected circuit to evaluate the device performance can be referenced from our previous work.[83] The V and I_{load} values in Figure 6d were collected after 2 min stabilizations of the multimeter-displayed values.

and 20 K. Here ω_{max} values are calculated by $\omega_{max} = \frac{P_{max}}{N \times A}$ (P_{max} is the maximum output power from Figure 6f and N is the number of thermoelectric legs, and A is the cross-sectional area of each leg). Notably, the PAM$_{0.3}$-BMIM:Cl$_{0.6}$-GO$_1$-based device exhibits an optimal ω_{max} of 1.32 mW cm^{-2} with a ΔT of 20 K. It should be noted that if the ionic thermoelectric material exhibits intermittent output voltage characteristics, the thermoelectric capacitor would be a more suitable device operating mode rather than a thermoelectric generator.[87]

3. Conclusion

In this study, we develop a novel ionic thermoelectric film with high flexibility, high stability, and high thermoelectric performance, composed of carbon-based materials (RO), ionic liquid, and cross-linked polymer. The film exhibits excellent thermoelectric properties with the S value of −76.7 mV K^{-1}, $S^2\sigma$ value of 753.0 μW m^{-1} K^{-2}, and ZT value of 0.19 at 383 K, which are highly competitive compared to existing ion thermoelectric materials. Additionally, the film demonstrates outstanding mechanical properties, including a tensile strength of 219.7 kPa, elongation at break of 389%, Young's modulus of 84.1 kPa, toughness of 0.4 MJ m^{-3}, and flexibility to bend at 180°. Importantly, the

film maintains its excellent thermoelectric and mechanical performance even after being placed in the air for 7 days. Based on these remarkable properties, we successfully fabricated a miniature 9-legged flexible thermoelectric device with dimensions of 25 × 25 mm^2, achieving a high optimized ω_{max} of 1.32 mW cm^{-2} with a ΔT of 20 K. This work provides a promising and novel approach for the long-term design of high-performance ion thermoelectric materials and easily integrable flexible devices.

4. Experimental Section

The experimental details are provided in the Supporting Information.

Supporting Information

Supporting Information is available from the Wiley Online Library or from the author.

Acknowledgements

Conflict of Interest

The authors declare no conflict of interest.

Data Availability Statement

The data that support the findings of this study are available from the corresponding author upon reasonable request.

Keywords

[1] X. Shi, L. Chen, *Nat. Mater.* **2016**, *15*, 691.

[2] Y. Xiao, L.-D. Zhao, *Science* **2020**, *367*, 1196.

[3] S. Roychowdhury, T. Ghosh, R. Arora, M. Samanta, L. Xie, K. Singh Niraj, A. Soni, J. He, V. Waghmare Umesh, K. Biswas, *Science* **2021**, *371*, 722.

[4] Q. Yang, S. Yang, P. Qiu, L. Peng, T.-R. Wei, Z. Zhang, X. Shi, L. Chen, *Science* **2022**, *377*, 854.

[5] W. B. Han, S.-Y. Heo, D. Kim, S. M. Yang, G.-J. Ko, G. J. Lee, D.-J. Kim, K. Rajaram, J. H. Lee, J.-W. Shin, T.-M. Jang, S. Han, H. Kang, J. H. Lim, D. H. Kim, S. H. Kim, Y. M. Song, S.-W. Hwang, *Sci. Adv.* **2023**, *9*, eadf5883.

[6] Z. Soleimani, S. Zoras, B. Ceranic, Y. Cui, S. Shahzad, *Nano Energy* **2021**, *89*, 106325.

[7] S.-W. Kim, J.-K. Kim, J. Y. Park, J. Mun, S. Jung, S. E. Yang, G. Lee, P. S. Lee, H.-C. Song, C. Yang, H. S. Park, J. S. Son, J. M. Baik, *Adv. Energy Mater.* **2023**, *13*, 2202987.

[8] H. Zhu, R. He, J. Mao, Q. Zhu, C. Li, J. Sun, W. Ren, Y. Wang, Z. Liu, Z. Tang, A. Sotnikov, Z. Wang, D. Broido, D. J. Singh, G. Chen, K. Nielsch, Z. Ren, *Nat. Commun.* **2018**, *9*, 2497.

[9] X.-L. Shi, J. Zou, Z.-G. Chen, *Chem. Rev.* **2020**, *120*, 7399.

[10] J. Sui, J. Li, J. He, Y.-L. Pei, D. Berardan, H. Wu, N. Dragoe, W. Cai, L.-D. Zhao, *Energy Environ. Sci.* **2013**, *6*, 2916.

[11] M. R. Burton, S. Mehraban, D. Beynon, J. McGettrick, T. Watson, N. P. Lavery, M. J. Carnie, *Adv. Energy Mater.* **2019**, *9*, 1900201.

[12] M. N. Hasan, M. Nafea, N. Nayan, M. S. Mohamed Ali, *Adv. Mater. Technol.* **2022**, *7*, 2101203.

[13] Y. Wang, L. Yang, X. Shi, X. Shi, L. Chen, M. Dargusch, J. Zou, Z.-G. Chen, *Adv. Mater.* **2019**, *31*, 1807916.

[14] T. Cao, X.-L. Shi, Z.-G. Chen, *Prog. Mater. Sci.* **2023**, *131*, 101003.

[15] J. L. Blackburn, A. J. Ferguson, C. Cho, J. C. Grunlan, *Adv. Mater.* **2018**, *30*, 1704386.

[16] C. Meng, C. Liu, S. Fan, *Adv. Mater.* **2010**, *22*, 535.

[17] N. Komatsu, Y. Ichinose, O. S. Dewey, L. W. Taylor, M. A. Trafford, Y. Yomogida, G. Wehmeyer, M. Pasquali, K. Yanagi, J. Kono, *Nat. Commun.* **2021**, *12*, 4931.

[18] K. Yusupov, A. Vomiero, *Adv. Funct. Mater.* **2020**, *30*, 2002015.

[19] C. Bounioux, P. Díaz-Chao, M. Campoy-Quiles, M. S. Martín-González, A. R. Goñi, R. Yerushalmi-Rozen, C. Müller, *Energy Environ. Sci.* **2013**, *6*, 918.

[20] G. Wu, Z.-G. Zhang, Y. Li, C. Gao, X. Wang, G. Chen, *ACS Nano* **2017**, *11*, 5746.

[21] B. Chen, Q. Chen, S. Xiao, J. Feng, X. Zhang, T. Wang, *Sci. Adv.* **2021**, *7*, eabi7233.

[22] C. Chi, M. An, X. Qi, Y. Li, R. Zhang, G. Liu, C. Lin, H. Huang, H. Dang, B. Demir, Y. Wang, W. Ma, B. Huang, X. Zhang, *Nat. Commun.* **2022**, *13*, 221.

[23] J. L.e Bideau, L. Viau, A. Vioux, *Chem. Soc. Rev.* **2011**, *40*, 907.

[24] Z. Liu, H. Cheng, H. He, J. Li, J. Ouyang, *Adv. Funct. Mater.* **2022**, *32*, 2109772.

[25] H. Wang, U. Ail, R. Gabrielsson, M. Berggren, X. Crispin, *Adv. Energy Mater.* **2015**, *5*, 1500044.

[26] S. Sun, M. Li, X.-L. Shi, Z.-G. Chen, *Adv. Energy Mater.* **2023**, *13*, 2203692.

[27] Z. A. Akbar, J.-W. Jeon, S.-Y. Jang, *Energy Environ. Sci.* **2020**, *13*, 2915.

[28] Z. Lei, W. Gao, P. Wu, *Joule* **2021**, *5*, 2211.

[29] W. B. Chang, C. M. Evans, B. C. Popere, B. M. Russ, J. Liu, J. Newman, R. A. Segalman, *ACS Macro Lett.* **2016**, *5*, 94.

[30] Y. Fang, H. Cheng, H. He, S. Wang, J. Li, S. Yue, L. Zhang, Z. Du, J. Ouyang, *Adv. Funct. Mater.* **2020**, *30*, 2004699.

[31] T. Li, X. Zhang, S. D. Lacey, R. Mi, X. Zhao, F. Jiang, J. Song, Z. Liu, G. Chen, J. Dai, Y. Yao, S. Das, R. Yang, R. M. Briber, L. Hu, *Nat. Mater.* **2019**, *18*, 608.

[32] H. Cheng, X. He, Z. Fan, J. Ouyang, *Adv. Energy Mater.* **2019**, *9*, 1901085.

[33] C.-G. Han, X. Qian, Q. Li, B. Deng, Y. Zhu, Z. Han, W. Zhang, W. Wang, S.-P. Feng, G. Chen, W. Liu, *Science* **2020**, *368*, 1091.

[34] T. Zhu, C. Jiang, M. Wang, C. Zhu, N. Zhao, J. Xu, *Adv. Funct. Mater.* **2021**, *31*, 2102433.

[35] S. Kee, M. A. Haque, D. Corzo, H. N. Alshareef, D. Baran, *Adv. Funct. Mater.* **2019**, *29*, 1905426.

[36] Z. Luo, W. Li, J. Yan, J. Sun, *Adv. Funct. Mater.* **2022**, *32*, 2203988.

[37] X. Xiao, M. Wang, S. Chen, Y. Zhang, H. Gu, Y. Deng, G. Yang, C. Fei, B. Chen, Y. Lin, M. D. Dickey, J. Huang, *Sci. Adv.* **2021**, *7*, eabi8249.

[38] F. Jiao, A. Naderi, D. Zhao, J. Schlueter, M. Shahi, J. Sundström, H. Granberg, J. Edberg, U. Ail, J. Brill, T. Lindström, M. Berggren, X. Crispin, *J. Mater. Chem. A* **2017**, *5*, 16883.

[39] B. Wu, Y. Guo, C. Hou, Q. Zhang, Y. Li, H. Wang, *Nano Energy* **2021**, *89*, 106487.

[40] J. Choi, Y. Jung, S. J. Yang, J. Y. Oh, J. Oh, K. Jo, J. G. Son, S. E. Moon, C. R. Park, H. Kim, *ACS Nano* **2017**, *11*, 7608.

[41] G. Wu, C. Gao, G. Chen, X. Wang, H. Wang, *J. Mater. Chem. A* **2016**, *4*, 14187.

[42] J. B. Ducros, N. Buchtová, A. Magrez, O. Chauvet, J. L.e Bideau, *J. Mater. Chem.* **2011**, *21*, 2508.

[43] H. Cheng, S. Yue, Q. Le, Q. Qian, J. Ouyang, *J. Mater. Chem. A* **2021**, *9*, 13588.

[44] Y. Wang, S. Kalytchuk, Y. Zhang, H. Shi, S. V. Kershaw, A. L. Rogach, *J. Phys. Chem. Lett.* **2014**, *5*, 1412.

[45] J. M. DeSimone, E. E. Maury, Y. Z. Menceloglu, J. B. McClain, T. J. Romack, J. R. Combes, *Science* **1994**, *265*, 356.

[46] K. P. Johnston, K. L. Harrison, M. J. Clarke, S. M. Howdle, M. P. Heitz, F. V. Bright, C. Carlier, T. W. Randolph, *Science* **1996**, *271*, 624.

[47] Y. Wang, Z. Shi, J. Yin, *ACS Appl. Mater. Interfaces* **2011**, *3*, 1127.

[48] Y. Si, E. T. Samulski, *Nano Lett.* **2008**, *8*, 1679.

[49] V. B. Mohan, R. Brown, K. Jayaraman, D. Bhattacharyya, *Mat. Sci. Eng. B* **2015**, *193*, 49.

[50] N. Yousefi, M. M. Gudarzi, Q. Zheng, S. H. Aboutalebi, F. Sharif, J.-K. Kim, *J. Mater. Chem.* **2012**, *22*, 12709.

**ADVANCED
SCIENCE NEWS**

www.advancedsciencenews.com

**ADVANCED
FUNCTIONAL
MATERIALS**

www.afm-journal.de

[51] P. Yang, K. Liu, Q. Chen, X. Mo, Y. Zhou, S. Li, G. Feng, J. Zhou, *Angew. Chem., Int. Ed.* **2016**, *55*, 12050.

[52] W. Gao, Z. Lei, W. Chen, Y. Chen, *ACS Nano* **2022**, *16*, 8347.

[53] H. Wang, D. Zhao, Z. U. Khan, S. Puzinas, M. P. Jonsson, M. Berggren, X. Crispin, *Adv. Electron. Mater.* **2017**, *3*, 1700013.

[54] J. Duan, G. Feng, B. Yu, J. Li, M. Chen, P. Yang, J. Feng, K. Liu, J. Zhou, *Nat. Commun.* **2018**, *9*, 5146.

[55] M. Bonetti, S. Nakamae, M. Roger, P. Guenoun, *J. Chem. Phys.* **2011**, *134*, 114513.

[56] S. L. Kim, J.-H. Hsu, C. Yu, *Nano Energy* **2018**, *48*, 582.

[57] D. Zhao, H. Wang, Z. U. Khan, J. C. Chen, R. Gabrielsson, M. P. Jonsson, M. Berggren, X. Crispin, *Energy Environ. Sci.* **2016**, *9*, 1450.

[58] W. Gao, Z. Lei, C. Zhang, X. Liu, Y. Chen, *Adv. Funct. Mater.* **2021**, *31*, 2104071.

[59] G. Wu, Y. Xue, L. Wang, X. Wang, G. Chen, *J. Mater. Chem. A* **2018**, *6*, 3376.

[60] Y. Li, Q. Li, X. Zhang, J. Zhang, S. Wang, L. Lai, K. Zhu, W. Liu, *Energy Environ. Sci.* **2022**, *15*, 5379.

[61] Z. Xu, Y. Bando, L. Liu, W. Wang, X. Bai, D. Golberg, *ACS Nano* **2011**, *5*, 4401.

[62] A. Sohn, C. Yu, *Mater. Today Phys.* **2021**, *19*, 100433.

[63] M. Jeong, J. Noh, M. Z. Islam, K. Kim, A. Sohn, W. Kim, C. Yu, *Adv. Funct. Mater.* **2021**, *31*, 2011016.

[64] M. Massetti, F. Jiao, A. J. Ferguson, D. Zhao, K. Wijeratne, A. Würger, J. L. Blackburn, X. Crispin, S. Fabiano, *Chem. Rev.* **2021**, *121*, 12465.

[65] Y. Liu, H. Wang, P. C. Sherrell, L. Liu, Y. Wang, J. Chen, *Adv. Sci.* **2021**, *8*, 2100669.

[66] D. M. Sayed, N. K. Allam, *J. Energy Storage* **2022**, *56*, 105882.

[67] A. Guo, H. Bai, Q. Liang, L. Feng, X. Su, G. Van Tendeloo, J. Wu, *Adv. Electron. Mater.* **2022**, *8*, 2200850.

[68] W. Cao, J. Zhang, K. Lin, J. Li, Y. Dong, D. Xia, R. Fan, Y. Yang, *Sol. RRL* **2022**, *6*, 2200310.

[69] S. Chen, X.j. Wang, L. Fan, G. Liao, Y. Chen, W. Chu, L. Song, J. Jiang, C. Zou, *Adv. Funct. Mater.* **2016**, *26*, 3532.

[70] W. Shen, H. Cai, Y. Kong, W. Dong, C. Bai, G. Liang, W. Li, J. Zhao, F. Huang, Y.-B. Cheng, J. Zhong, *Small* **2023**, *19*, 2302194.

[71] J. Xu, H. Wang, X. Du, X. Cheng, Z. Du, H. Wang, *ACS Appl. Mater. Interfaces* **2021**, *13*, 20427.

[72] I. H. Sajid, M. F. M. Sabri, S. M. Said, M. F. M. Salleh, N. N. N. Ghazali, R. Saidur, B. Subramaniam, S. W. Hasan, H. A. Jaffery, *Energ. Convers. Manage* **2019**, *198*, 111813.

[73] X. Lu, Y. Mi, *Macromolecules* **2005**, *38*, 839.

[74] X. Zhang, G. Zhang, X. Huang, J. He, Y. Bai, L. Zhang, *ACS Appl. Mater. Interfaces* **2022**, *14*, 30256.

[75] S. He, G. Wang, Z. Zhao, *Catal. Sci. Technol.* **2023**, *13*, 3489.

[76] H. Lee, S. Chae, H. Jo, S. Kim, M. Kim, J. Lee, S. Lee, C. S. Park, H. Yoon, *ACS Appl. Nano Mater.* **2022**, *5*, 15962.

[77] K. Krishnamoorthy, M. Veerapandian, K. Yun, S. J. Kim, *Carbon* **2013**, *53*, 38.

[78] Z. Zhao, R. Pu, Z. Wang, J. Jiang, W. Liu, *J. Phys. Chem. C* **2023**, *127*, 3516.

[79] D. W. Chang, E. K. Lee, E. Y. Park, H. Yu, H.-J. Choi, I.-Y. Jeon, G.-J. Sohn, D. Shin, N. Park, J. H. Oh, L. Dai, J.-B. Baek, *J. Am. Chem. Soc.* **2013**, *135*, 8981.

[80] R. Al-Gaashani, A. Najjar, Y. Zakaria, S. Mansour, M. A. Atieh, *Ceram. Int.* **2019**, *45*, 14439.

[81] L. Stobinski, B. Lesiak, A. Malolepszy, M. Mazurkiewicz, B. Mierzwa, J. Zemek, P. Jiricek, I. Bieloshapka, *J. Electron Spectrosc. Relat. Phenom.* **2014**, *195*, 145.

[82] Y. Zhang, J. He, P.-N. Wang, J.-Y. Chen, Z.-J. Lu, D.-R. Lu, J. Guo, C.-C. Wang, W.-L. Yang, *J. Am. Chem. Soc.* **2006**, *128*, 13396.

[83] S. Sun, X.-L. Shi, M. Li, T. Wu, L. Yin, D. Wang, Q. Liu, Z.-G. Chen, *ACS Appl. Mater. Interfaces* **2023**, *15*, 25650.

[84] M. C. M. Rodrigues, M. Militzer, *Mater. Charact.* **2020**, *163*, 110273.

[85] E. J. Payton, P. J. Phillips, M. J. Mills, *Mat. Sci. Eng. A* **2010**, *527*, 2684.

[86] S. Yang, P. Qiu, L. Chen, X. Shi, *Small Sci* **2021**, *1*, 2100005.

[87] Y. Li, Q. Li, X. Zhang, B. Deng, C. Han, W. Liu, *Adv. Energy Mater.* **2022**, *12*, 2103666.